Journal of Materials Chemistry A

PAPER

View Article Online
View Journal | View Issue

Cite this: J. Mater. Chem. A, 2016, 4, 14865

Ligand-free nano-grain Cu_2SnS_3 as a potential cathode alternative for both cobalt and iodine redox electrolyte dye-sensitized solar cells†

Feng Liu,[ab] Shuanglin Hu,[c] Xunlei Ding,[a] Jun Zhu,*[b] Jian Wen,[b] Xu Pan,[b] Shuanghong Chen,[b] Md. K. Nazeeruddin[d] and Songyuan Dai*[ab]

Received 12th July 2016
Accepted 30th August 2016

DOI: 10.1039/c6ta05871j

www.rsc.org/MaterialsA

Tetragonal phase Cu_2SnS_3 (CTS) in the form of nano-grain thin film serves as an efficient inexpensive electrocatalyst alternative to the commonly used Pt in dye-sensitized solar cells (DSSCs) exhibiting remarkable electrochemical stability and electrocatalytic activity for both cobalt (Co(III)/Co(II))- and iodine (I_3^-/I^-)-based redox electrolytes. In this study, the catalytic activity of the CTS electrode was first theoretically predicted *via* first-principles calculations using density functional theory. Electrochemical measurements confirm their superior catalytic performance to Pt toward both the reduction of I_3^- and Co^{3+}. Significantly, ensuing DSSCs with the CTS cathode demonstrate a photovoltaic efficiency of 10.26%, higher than that with Pt (9.31%). Through impedance spectra, we also show that increasing the amount of CTS loading can further enhance its apparent catalytic performance. However, improving the crystallization of the CTS film by increasing the annealing temperature to a certain degree will only reduce its activity.

Introduction

Over the past 20 years, dye-sensitized solar cells (DSSCs) have attracted tremendous attention in both scientific research and industrial applications because of their low cost, ease of fabrication, stable power output, and short energy payback.[1] Impressive solar-to-electrical energy conversion efficiency (>14%) has been achieved after several years of development, rendering them credible alternatives to the conventional solid-state devices.[2–4] The counter electrode (CE) constitutes one of the most important components in DSSCs and functions to catalyze the reduction of the redox couple in electrolytes. The champion DSSC devices nowadays with the highest efficiency employ a cobalt (Co(III)/Co(II))-based electrolyte.[2–4] Compared to the traditional iodide/triiodide (I_3^-/I^-) redox couple, these cobalt-based redox shuttles are non-volatile, non-corrosive, and weakly colored. Moreover, cobalt-based redox shuttle mediators generally allow for a higher achievable open-circuit voltage due to their more positive redox potential.[5,6] Besides, their long-term stability has also been significantly improved after several years of development.[6,7] However, like the I_3^-/I^- redox system, most Co-mediated DSSCs still use the precious platinum (Pt) as their cathode,[8,9] and there are actually very limited alternatives that perform well with the electrolyte.[10] Practical advantages of DSSCs can be gained by reducing the cost of the CE, which has also long been a critical issue in DSSC research. For the sake of cost control and competitive effectiveness, researchers have strived to develop alternative CEs being more efficient and cost-effective for both electrolytes.[11–13] Just recently, Wu's group reported a highly effective Co_3S_4/electrospun-carbon-nanofibers composite CE, showing good performance in $Co^{3+/2+}$ DSSCs.[13] Notably, the choice of the CE material is different for certain redox systems.[14] Herein, we report low-cost Cu_2SnS_3 (CTS) thin film CEs with iodine as well as cobalt redox electrolyte DSSCs.

Earth-abundant and low-toxicity chalcogenide CTS has emerged as an attractive candidate for use in next generation photovoltaic cells, electrochemical devices, and photocatalytic energy conversion schemes.[15–17] In particular, semiconductor CTS exhibits excellent electrical conductivity (*ca.* 0.66–3.43 Ω^{-1} cm^{-1}) and high chemical stability,[18,19] making it highly attractive and advantageous for both electrochemical and electrocatalytic applications. For example, Qu *et al.* prepared cabbage-like nanostructured CTS and used them as a potential anode in lithium batteries.[20] Lee's group reported CTS functions as an efficient catalyst in quantum dot solar cells.[21] Compared

[a]Beijing Key Laboratory of Novel Thin Film Solar Cells, State Key Laboratory of Alternate Electrical Power System with Renewable Energy Sources, North China Electric Power University, Beijing, 102206, P. R. China. E-mail: sydai@ipp.ac.cn

[b]Key Laboratory of Novel Thin Film Solar Cells, Institute of Applied Technology, Hefei Institutes of Physical Science, Chinese Academy of Sciences, Hefei, 230031, P. R. China. E-mail: zhujzhu@gmail.com

[c]Institute of Nuclear Physics and Chemistry, China Academy of Engineering Physics, Mianshan Road 64, Mianyang 621900, Sichuan, P. R. China

[d]Laboratory for Photonics and Interfaces, Institute of Chemical Sciences and Engineering, School of Basic Science, Swiss Federal, Institute of Technology, CH-1015 Lausanne, Switzerland

† Electronic supplementary information (ESI) available. See DOI: 10.1039/c6ta05871j

with the previously proposed multinary chalcogenide catalysts such as $Cu_2ZnSnS_4Se_{4-x}$ (ref. 22) and Cu_2FeSnS_4 (ref. 23), ternary CTS is more attractive in practical applications due to its compositional simplicity. However, to the best of our knowledge, there are no reports on a CTS cathode in conjunction with a Co-mediated DSSC and there is only one report on I_3^-/I^- DSSCs with CTS material, where colloidal CTS nanocrystals with a cubic phase were *in situ* grown on a Mo substrate and used as an alternative catalyst to Pt.[24] Yet the power conversion efficiency (PCE) was quite low (3.35%) and direct comparison with the Pt cathode was not made in that paper. It is known that colloidal nanocrystals have an inorganic core that is typically stabilized by a surface layer of organic ligands.[25] However, previous studies have indicated that the insulating nature of these long organic surfactants imposes limitations on charge transport within the nanostructured films because of the poor interparticle coupling.[26,27] If this is the case, it would dramatically deteriorate the electrical conductivity of the resulting thin films and, consequently, the catalytic performance.[10,28] Additionally, the catalytic performance of a thin film catalyst also strongly depends on its crystal structures, surface properties, and film morphologies (*e.g.*, film thickness, particle size, and shape), which are closely associated with the employed synthesis techniques.[11,29]

The aim of this work is to fabricate low-cost CTS using an environmentally benign route, and explore its potential use as an efficient CE catalyst in DSSCs. A hydrazine-based chemical route to ligand-free chalcogenide films (*e.g.*, $Cu_2ZnSn(S,Se)_4$ and $Cu(In,Ga)(Se,S)_2$) has made great success in recent years and has recently been employed to prepare CTS thin films for photovoltaic applications.[18,30,31] The achievement, however, comes at the expense of the use of hydrazine, which is highly toxic, carcinogenic, and potentially explosive, thereby unfavorable to use on a large scale. Most recently, Brutchey's group has shown that a relatively safer two-component thiol-amine solvent mixture has a strong ability to dissolve a series of binary chalcogenides, for instance, Bi_2S_3, Sb_2S_3, As_2Te_3, Bi_2Se_3, and Sb_2Se_3, forming molecular chalcogenide complexes that can be easily recovered to semiconducting phases upon gentle heat treatment.[32] In this study, a thiol-amine solvent mixture-based route was developed and employed to produce our ligand-free ternary CTS thin films, *i.e.* Cu_2S and SnS_2 powders were stoichiometrically dissolved in a mixture of ethylenediamine and ethanedithiol, forming homogeneous precursor solution that yielded crystalline CTS upon annealing. The precursor solution-based method is robust and efficient, it is less time consuming than the conventional colloidal synthesis of nanocrystals and much simpler than the physical vapor deposition approaches which typically require high-vacuum conditions and more sophisticated equipments,[23,33,34] allowing a much reduced manufacturing cost and facilitating large-scale production of CTS thin films. It is worth mentioning that with similar synthesis techniques, several kinds of chalcogenide films (*e.g.*, CuSe and Cu_2SnSe_3) have been previously prepared and used as potential electrocatalysts in sulfide/polysulfide (S_n^{2-}/S^{2-}) redox systems.[35,36] However, we found that these materials decomposed or detached from the substrate during electrochemical cycling in the I_3^-/I^- and/or Co(III)/Co(II) redox electrolyte, thus they are not suitable for use in DSSCs. In contrast, the CTS thin film electrode exhibits impressive mechanical robustness and remarkable electrochemical stability in the above two electrolytes. This is of particular importance when further evaluating their applicability as CEs in DSSCs. For the first time, in this paper, through theoretical calculations using density functional theory (DFT) and experimental measurements by electrochemical methods we show that the CTS electrode in the form of nano-grain thin film possesses excellent electrocatalytic ability toward both the iodine and cobalt electrolytes. Under optimal conditions, the CTS CE exhibits better electrochemical activity than Pt with respect to its lower charge transfer resistance in both electrolytes (less than 1 Ω cm^2 can be achieved), enabling optimal output performance for Pt-free DSSCs. Ensuing DSSCs with the CTS cathode demonstrate a photovoltaic efficiency of 10.26%, higher than that with Pt (9.31%), which is one of the highest efficiencies ever reported for Pt-free DSSCs to date.[37]

Experimental section

Counter electrode preparation

The CTS CE was prepared using the following procedure. First, 0.1 M CTS precursor solution was prepared by simultaneously dissolving 0.5 mmol of Cu_2S (99.5%, Alfa Aesar) and 0.5 mmol of SnS_2 (99.99%, Apollo Scientific Limited.) powders in 5 mL of 10 : 1 vol/vol 1,2-ethylenediamine (en) and 1,2-ethanedithiol ($edtH_2$) by overnight magnetic stirring at 60 °C. Then the precursor solution was coated onto a pre-cleaned (using deionized water, acetone, and ethanol) fluorine-doped tin oxide (FTO) glass substrate by spin coating at 3000 rpm for 30 s. A uniform semitransparent yellow film was obtained after drying at 120 °C. The film was finally annealed at 320 °C for 15 min. After cooling, it can be directly used as a cathode in DSSCs. All of the processes were performed in a nitrogen-filled glovebox. The reference Pt electrode was prepared by deposition of *ca.* 3 μL cm^{-2} of 5 mM H_2PtCl_6/2-propanol solution on an FTO glass, and it was then sintered in a muffle furnace at 450 °C for 30 min.

Solar cell fabrication

Screen-printed TiO_2 double layer electrodes with a mesoporous layer (12 μm) and a superimposed light-scattering layer (6 μm) were prepared according to our previous study.[38] Prior to use, the TiO_2 electrodes were placed in a 40 mM $TiCl_4$ aqueous solution at 70 °C for 30 min, and thereafter sintered at 510 °C for 30 min in air. Dye adsorption of the photoanode was carried out by immersing the TiO_2 electrodes (when it was cooled to 100 °C) in an acetonitrile solution containing 0.3 mM C101 dye (which was kindly provided by Prof. Peng Wang) for 12 h. The triiodide/iodide (I_3^-/I^-) electrolyte for DSSCs was prepared using 0.03 M I_2, 0.06 M LiI, 0.5 M *tert*-butylpyridine, 0.6 M 1-butyl-3-methylimidazolium iodide, and 0.1 M guanidinium thiocyanate in anhydrous acetonitrile. Co(III)/Co(II) electrolyte solution was 0.22 M $Co(L)_2(PF_6)_2$, 0.05 M $Co(L)_2(PF_6)_3$, 0.1 M $LiClO_4$, and 0.2 M 4-*tert*-butylpyridine in acetonitrile. L is 6-(1*H*-

pyrazol-1-yl)-2,2′-bipyridine. Sandwich solar cells were fabricated using the sensitized TiO_2 film as a working electrode and the Pt or CTS-coated FTO glass as a CE. The two electrodes were assembled by heating using a thermal adhesive film (Surlyn, 60 μm, Dupont), which also served as a spacer between the electrodes. The electrolyte was then driven into the cell through a drilled hole in the CE by vacuum backfilling followed by sealing with a Surlyn film and a cover glass to avoid leakage of the electrolyte. The effective cell area was 0.25 cm^2, as defined by a mask.

Characterization

Thermo-gravimetric analysis (TGA) was carried out on TGA Q5000IR equipment (TA Instruments, USA). Fourier transform infrared spectroscopy (FT-IR) was performed on a Nicolet 8700 FTIR spectrometer (USA). The phase identification was carried out using powder X-ray diffraction (XRD, TTR-III, Rigaku Corp., Japan). The morphology and crystal structure of the prepared films were characterized using field emission scanning electron microscopy (FESEM, FEI, Quanta 200FEG) and high-resolution transmission electron microscopy (HRTEM, JEM-2100F, Japan). Energy dispersive X-ray spectroscopy (EDS) was performed with an energy dispersive spectrometer equipped on the SEM/TEM equipment. Inductively coupled plasma atomic emission spectrometry (ICP-AES) was performed on a Perkin-Elmer Optima 3000DV after dissolving the nanocrystals in aqua regia. Tapping-mode atomic force microscopy (AFM) was conducted with a Dimension Icon AFM (Bruker AXS, Germany). UV-vis absorption spectra were obtained with a spectrophotometer (HITACHI, U-3900H, Japan). Cyclic voltammetry (CV) measurement was performed in a three-electrode system using a nitrogen-purged electrolyte containing 0.1 M $LiClO_4$, 10 mM LiI, and 1 mM I_2 in acetonitrile, a Pt mesh used as the counter electrode and an Ag/AgCl electrode serving as the reference electrode. Electrochemical impedance spectroscopy (EIS) was carried out using a symmetrical dummy cell at an applied bias of 0 V, the modulation frequency ranging from 0.01 Hz to 100 kHz with a 5 mV ac amplitude. Dummy cells were fabricated by sandwiching two identical electrodes with the same redox electrolyte as used in the solar cells filled in-between (*i.e.*, CE//electrolyte//CE). Tafel polarization curves were measured on the dummy cells with a scan rate of 50 mV s^{-1}. The geometric surface area of the symmetrical cells with a mask was 0.56 cm^2. All the electrochemical measurements were conducted on an electrochemical workstation (Autolab 302N, Metrohm, Switzerland) and the data were recorded at room temperature. The BET specific surface area of the samples was measured in a nitrogen adsorption–desorption apparatus (Tristar 3020, Micromeritics). *J–V* characteristics of the solar cells were derived with a Keithley 2420 digital source meter (Keithley, USA) under a 450 W xenon lamp (Oriel Sol3A Solar Simulator 94043, Newport Stratford Inc., USA).

Computational details

We calculated the adsorption energies of one iodine atom on the Cu_2SnS_3 (112) surface in various configurations by employing density functional theory (DFT). The plane-wave basis-set and periodic boundary condition code package of Vienna *ab initio* Simulation Package (VASP) are used.[39,40] The spin-polarized calculations were performed with the Perdew–Burke–Ernzerhof (PBE)[41] version of gradient-generalized approximation (GGA) functional. The valence-core election interaction was described by the projector augmented-wave (PAW)[42] method. The energy cutoff for plane-wave basis-set expansion was set to 400 eV. The Cu_2SnS_3 (112) surface model was built from the bulk tetragonal Cu_2SnS_3 structure with the experimental lattice parameter $a = 5.41$ Å and $c = 10.82$ Å.[43] Similar to the other phases of Cu_2SnS_3, the tetragonal Cu_2SnS_3 structure is actually a perturbation of the cubic zinc-blend phase structure due to the disorder distribution of the Cu and Sn atoms.[44] While the lattice vectors of the cubic phase are ($e\rightharpoonup_x$, $e\rightharpoonup_y$, $e\rightharpoonup_z$), the tetragonal phase lattice vectors are $a\rightharpoonup = e\rightharpoonup_x$, $b\rightharpoonup = e\rightharpoonup_y$, $c\rightharpoonup = 2e\rightharpoonup_z$, respectively. As also pointed out in Zhai *et al.*'s study,[44] in the Cu_2SnS_3 structures, the Cu_3Sn and Cu_2Sn_2 tetrahedral clusters are energy favored over the others, thus only these two clusters surrounding the central S atom are presented in our model, and several representative combinations of these two structures are exposed on the top layer of the (112) surface slab model. The adopted (112) surface slab model is in the box of size 15.31 Å × 13.26 Å × 35.00 Å, which contains 64 Cu, 32 Sn and 96 S atoms. It holds the in-plane periodicity of $2\sqrt{2}e_x \times \sqrt{6}e_x$, that is 15.31 Å × 13.26 Å, and six Cu–Sn–S layers (with the total thickness of 18.75 Å before relaxation) in the surface normal direction, and a vacuum layer larger than 15 Å to prevent the virtual interaction between repeated images. The dipole correction was applied in the surface normal direction. The bottom most Cu–Sn–S layer was fixed while all the other atoms were relaxed before the energies were calculated. Only the Γ-point was used for the Brillouin zone integration since the supercell size was large. The geometries were relaxed until the forces on the atoms were smaller than 0.02 eV $Å^{-1}$, and the energy convergence criterion was 10^{-5} eV per cell. The Cu_2SnS_3 (112) surface is a polar surface, which could be stabilized by geometric reconstruction. After the relaxation, the Cu and S atoms in the top layer moved to the same plane, while all the Sn and one S atoms moved above (Fig. S1, ESI†). We then tested all the possible adsorption sites on this surface for one iodine atom (I) or one CH_3CN adsorption. We increased the number of adsorbed CH_3CN molecules around the iodine in a stepwise manner, based on the lowest energy configuration with one less CH_3CN determined in the last step. The adsorption structures were optimized and the adsorption energy was calculated according to:

$$E_{ad}^{I} = E_{tot}(I/surface) - E_{tot}(surface) - \frac{1}{2}E_{tot}(I_2, gas)$$

where E_{tot}(I/surface), E_{tot}(surface), and E_{tot}(I_2, gas) are the energies of the I atom adsorbed on the Cu_2SnS_3 surface system, the pure surface with the same number of adsorbed CH_3CN molecules, and I_2 in the gas phase, respectively. The more negative E_{ad}^{I} is, the more strongly the species I binds on the surface.

Results and discussion

The first step of the solvent mixture route to CTS films consists of stoichiometrically dissolving Cu_2S and SnS_2 powders into a mixture of ethylenediamine and ethanedithiol, forming homogeneous precursor solution by overnight magnetic stirring at 60 °C. The solution is then spin-coated onto a FTO glass to form the precursor film, with the layer thickness being controlled by the solution concentration, spin speed, and ramp rate (see Experimental section for details). Heat treating the precursor film leads to the removal of the excess solvent from the sample. With the increase of temperature, some decomposition of the precursor film will have commenced. The transition from the precursor film to the single-phase nanocrystal is completed with a final high temperature treatment at 320 °C for a period of time (typically 20 min). Thermogravimetric analysis (TGA) was used to determine this final temperature, at which point the CTS precursors were nearly completely decomposed (Fig. S2†). The formation of the CTS was indicated by the change of the film color from yellow to brown and can also be verified by the complete removal of the organic species in the final product (see FT-IR spectra in Fig. S3†). The product on FTO glass shows a mirror-like surface, indicating its excellent uniformity and smoothness. Also, these thin films exhibit impressive mechanical robustness that they do not detach from the glass even on sonicating in water for hours. The crystal structure of the resulting thin films was first characterized by X-ray diffraction (XRD) measurement. The main diffraction peaks of the sample located at 28.50°, 47.48°, and 56.30° shown in Fig. 1a can be well-indexed to the (112), (204), and (312) crystal planes of the tetragonal ($I\bar{4}2m$) CTS phase (JCPDS Card no. 89-4714).[45] No unidentified peaks were observed in the XRD data, demonstrating well-crystallized and single phase films. In order to further study and confirm the structure types of the obtained films, Raman spectra of the powder sample are recorded in Fig. 1b. The spectrum is characterized by the presence of two dominant peaks at 294 cm^{-1} and 332 cm^{-1}, which matches with those found for tetragonal CTS in previous studies.[46,47] The chemical composition of the as-prepared films was examined by inductively coupled plasma atomic emission spectrometry (ICP-AES), which showed a Cu/Sn/S atomic ratio of 1.98 : 1.00 : 3.03, close to the ideal stoichiometry ratio of the Cu_2SnS_3 semiconductor. Scanning transmission electron microscopy-energy dispersive spectroscopy (STEM-EDS) elemental maps and line scan (Fig. 1c and d) further confirm that the three elements are homogeneously distributed in the resulting crystals. The above results indicate the successful formation of the tetragonal phase crystalline CTS from solution. Based on a previous discussion about the dissolution power of the ethylenediamine (en)/ethanedithiol ($edtH_2$) binary solvent,[32] we propose the following reactions (1–3) for the formation of our ternary CTS. Reaction (1) describes the formation of ionic species upon mixing $edtH_2$ and en. Further, as indicated, dissolving chalcogenide powder in this solvent mixture forms en-ligated

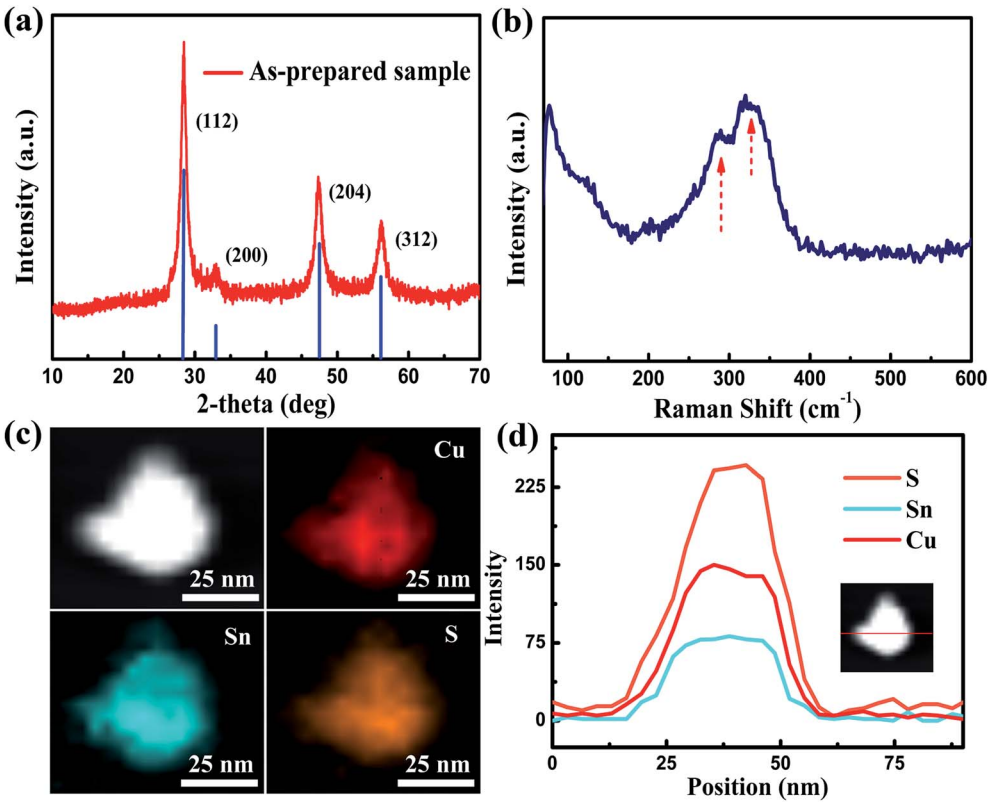

Fig. 1 (a) Powder XRD patterns of the annealed sample. (b) Raman spectrum of the obtained thin film recorded in the spectral range of 50–600 cm^{-1}. A final temperature at 320 °C was employed here. (c) STEM image and STEM-EDS elemental mappings of the CTS nanoparticles. (d) STEM-EDS line scan of one single CTS nanoparticle.

thiolatochalcogenometallate anions that are counterbalanced by enH^+ cations, demonstrating that the intermediate product $(enH^+)_6[Cu_2Sn(edt)_3S_3]^{6-}(en)_3$ exists in the solvent, as described by reaction (2) (but further work is required to confirm this product). Finally, solid thin film is obtained upon gentle heat treatment of the precursors on the FTO glass (reaction (3)).

$$3en + (edt)H_2 \rightarrow (enH^+)_2(edt^{2-})(en) \quad (1)$$

$$Cu_2S + SnS_2 + 3(enH^+)_2(edt^{2-})(en) \rightarrow (enH^+)_6[Cu_2Sn(edt)_3S_3]^{6-}(en)_3 \quad (2)$$

$$(enH^+)_6[Cu_2Sn(edt)_3S_3]^{6-}(en)_3 \triangleq Cu_2SnS_3 + 9en\uparrow + 3(edt)H_2\uparrow \quad (3)$$

In fact, we have also tested the other solvents with mixtures of, for example, ethylenediamine with thioglycolic acid, or ethanolamine with thioglycolic acid. All these binary solvent mixtures possess a 1,2-dithiol/1,2-diamine functionality and they showed good solvent ability for Cu_2S and SnS_2 powders. However, it was found that the resulting thin films from these solvents exhibit different grain sizes and crystal structures.

The morphologies and structures of the resulting thin films were examined by scanning electron microscopy (SEM), atomic force microscopy (AFM), and transmission electron microscopy (TEM). Fig. 2a shows the representative high-magnification TEM image of the tetragonal CTS nanoparticles. The clear lattice fringes with a distance of 0.31 nm are consistent with the *d*-spacing of the (112) crystallographic plane of CTS.[45] The cross-section SEM image (Fig. 2b) indicates that CTS thin film has a dense and continuous surface with a thickness of about 70 nm. Its nonporous surface can thus be demonstrated. Therefore, diffusion of the electrolyte in pores can be neglected. Fig. 2c and S4a† show typical low-magnification surface SEM

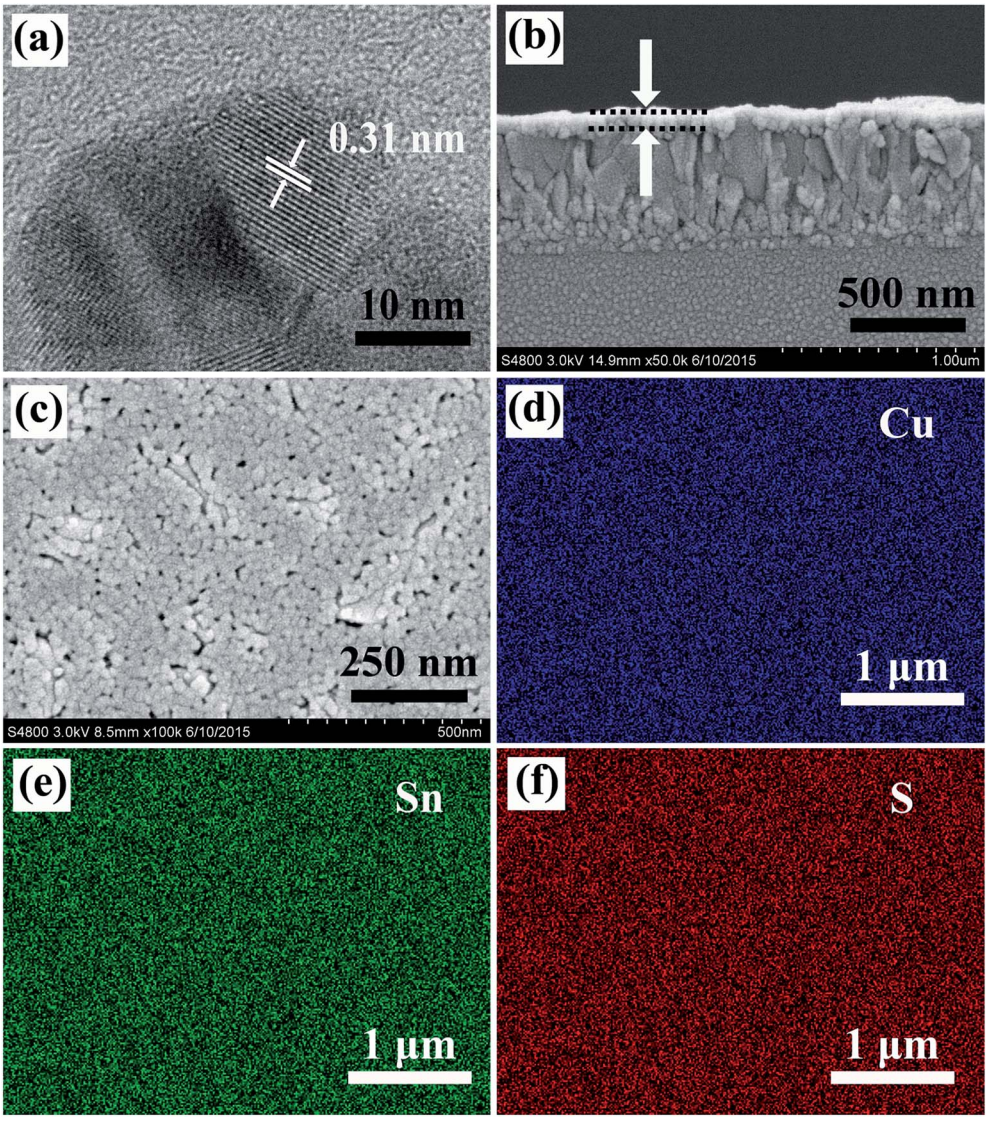

Fig. 2 (a) High-resolution TEM image of CTS nanoparticles. (b) Cross-section SEM image and (c) surface SEM image of CTS thin film on a FTO glass. (d–f) Elemental mapping of copper (d), tin (e), sulfur (f) recorded by EDS spectroscopy.

images of the resulting films. Despite the uniform and compact nature confirmed by its cross-section image, a few voids in the film were observed in Fig. 2c, which can be attributed to the aggregation of CTS nanoparticles during sintering. It is observed that the CTS nanoparticles have the size of 20–30 nm in diameter and they are closely packed to form the CTS films. Combined with the cross-section observation in Fig. 2b, this feature indicates that the FTO substrate was in fact covered by just 2–3 CTS nanoparticle layers. Fig. S4b† shows a typical tapping-mode AFM image of the CTS film surface with the mean and the rms roughness of 17.97 and 22.87 nm, respectively. The grain size estimated from AFM (~25 nm) is consistent with the grain size observed in SEM images. To further confirm the elemental distribution of the as-synthesized CTS thin films, SEM-EDS elemental maps (Fig. 2d–f) were recorded, revealing the homogeneous distribution of all three elements. Therefore, the above results of XRD, Raman, SEM, and TEM analyses indicate that the CTS was successfully deposited in the form of nano-grain thin films without the necessity of complex colloidal synthesis of nanocrystals and also, our procedure introduced here is much safer than those based on hydrazine.

As proposed in Hou *et al.*'s study, the catalytic activity of one electrode surface to the I_3^-/I^- reactions can be evaluated from the adsorption energy of one iodine atom (I) on the catalyst surfaces.[48] With the details presented in the above Experimental section, we found that the adsorption of I on the tetragonal Cu_2SnS_3 (112) surface with the E_{ad}^{I} varies from 0.50 eV to 0.95 eV depending on the adsorption sites but with a slight preference on the Sn site (Table S1†). While the CH_3CN molecule prefers the Cu site (Table S2†), more CH_3CN molecules are put on the Cu sites around the lowest energy I adsorption configuration. With the number of adsorbed CH_3CN increasing, the adsorption of I is first strengthened and then weakened (Table S3†), but most of the cases fall well in the optimum range of 0.33–1.20 eV for good catalysts.[48] It indicates the general good electrocatalytic activity of this surface with little dependence on the structure of solvated I/CH_3CN.

In order to test and verify our deduction, we next performed Tafel polarization analysis to investigate the electrochemical activity of the prepared CTS cathodes for the I_3^-/I^- redox couple by using a symmetrical dummy cell. A Pt-coated electrode served as the reference. Fig. 3a shows the Tafel polarization curves of the two electrodes. The extrapolated intercepts of the

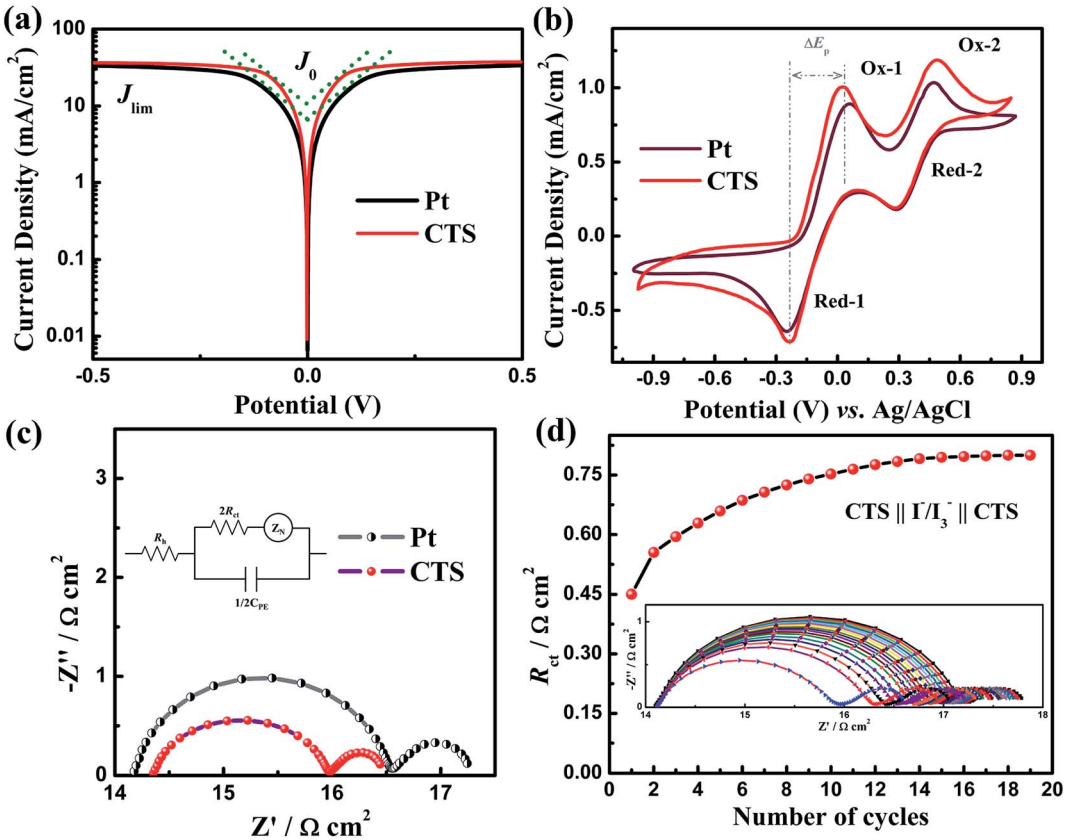

Fig. 3 (a) Tafel polarization curves of the Pt and CTS symmetrical cells. (b) Cyclic voltammograms of I_3^-/I^- redox species for the Pt and CTS electrodes. The scan rate was set to 20 mV s^{-1}, room temperature was 25 °C. (c) Nyquist plots from the EIS measurements of the Pt and CTS symmetrical cells. The inset shows the equivalent circuit for fitting the EIS spectra. R_h: sheet resistance of the CE; R_{ct}: charge transfer resistance between the CE and the electrolyte; Z_N: Nernst diffusion impedance of the electrolyte; C_{PE}: constant phase element of the electrical double layer. (d) Stability test by plotting the evolution of R_{ct} of the CTS CE with accelerated degradation EIS measurements of the symmetrical cells. The sequence of measurements was as follows: twice cyclic voltammetry scans from 0 V → 1 V → −1 V → 0 V (scan rate 50 mV s^{-1}) with a 20 s relaxation at 0 V followed by EIS measurement at 0 V from 100 kHz to 0.01 Hz.

anodic and cathodic branches of the Tafel polarization curves (labeled in Fig. 3a) indicate the exchange current density (J_0), which can be calculated by eqn (1),

$$J_0 = \frac{RT}{nFR_{ct}} \quad (1)$$

where R is the gas constant, n is the number of electrons involved in the electrochemical reduction of I_3^- at the electrode, F is the Faraday's constant, R_{ct} is the charge transfer resistance between the interface of the electrolyte and the CE. In general, the evaluation of the R_{ct} value is very important to determine the quality of a catalytic electrode and the lower R_{ct} value corresponds to a better catalytic activity of a CE. Obviously, J_0 varies inversely with R_{ct} and the CTS electrode presents a larger slope for the Tafel curve, suggesting a higher J_0 value and thus a smaller R_{ct} on the CTS electrode. In addition, from the Tafel polarization curves, we can also gain information about the limiting current density (J_{lim}), the intersection of the cathodic branch with the Y-axis. J_{lim} is directly proportional to the diffusion coefficient (D_n) of the redox couple in the electrolyte in terms of eqn (2),

$$J_{lim} = \frac{2nFcD_n}{l} \quad (2)$$

where c is the concentration of I_3^-, l is the space thickness of the symmetric cells, n and F retain their established meanings. It is observed that the J_{lim} value of the CTS electrode is slightly higher than that of Pt and hence corresponds to a larger D_n, inferring that D_n increases with increasing catalytic activity of the electrode. This observation is consistent with the previously reported behavior.[49]

Cyclic voltammetry was conducted to further investigate the catalytic performance of the CE. Fig. 3b shows the CV curves of the CTS and Pt electrodes that performed in a three-electrode system in the I_3^-/I^- electrolyte. Both electrodes exhibit two typical pairs of oxidation-reduction peaks. The left one in the low potential range corresponds to the oxidation (Ox-1, $3I^- \rightarrow I_3^- + 2e^-$) and reduction (Red-1, $I_3^- + 2e^- \rightarrow 3I^-$) of I_3^-/I^-, whereas the right one in the high potential range can be assigned to the oxidation (Ox-2, $2I_3^- \rightarrow 3I_2 + 2e^-$) and reduction (Red-2, $3I_2 + 2e^- \rightarrow 2I_3^-$) peaks of I_2/I_3^-. Since a DSSC CE mainly catalyzes the reduction of I_3^- to I^-, the catalytic activity of the electrode can be evaluated from the peak current density and the peak-to-peak separation (E_{pp}) of Ox-1 and Red-1 peaks.[11,50] E_{pp} is negatively correlated with the standard electrochemical rate constant of a redox reaction, *i.e.*, the lower the E_{pp} value, the better the catalytic activity is.[51] As expected, it is found that the E_{pp} of the CTS electrode (*ca.* 260 mV) is slightly smaller than that of Pt (340 mV) and is directly responsible for the fact that the overpotential loss of the CTS CE is lower than that of the Pt CE in DSSCs. Interestingly, the resulting E_{pp} value of our CTS is quite close to the value reported in the literature for a high-performance graphene CE (compared under the same conditions, *e.g.*, bias voltage, scan rate).[52] What's more, the higher peak current densities of the CTS electrode further confirm its higher catalytic activity toward the reduction of I_3^-.

The charge transfer process at the interface between the CTS electrode and the electrolyte was more accurately characterized by electrical impedance spectroscopy (EIS). EIS spectra (Fig. 3c) of the symmetric cells can directly provide the parameters of the impedance properties of a CE, *i.e.*, sheet resistance of the electrode, R_h (high frequency around 100 kHz), R_{ct} (frequency region between 1 kHz and 100 kHz), and Nernst diffusion impedance of the electrolyte, Z_N (from 0.01 Hz to 1 kHz). The values of R_h, R_{ct}, and Z_N obtained by fitting the EIS spectra (the inset in Fig. 3c shows the equivalent circuit for fitting this type of cell) are 14.2, 0.45, and 0.5 Ω cm^2 for CTS, respectively, and 14.0, 0.75, and 0.8 Ω cm^2 for Pt, respectively. The decrease in Z_N can be rationalized in terms of eqn (3), which indicates that Z_N tends to decrease with the increase of D_n.

$$Z_N = \frac{kT}{n^2q^2cA\sqrt{i\omega D_n}}\tanh\left(\sqrt{\frac{i\omega}{D_n}}l\right) \quad (3)$$

where A is the electrode area, q is the elementary charge, k is the Boltzmann constant, and ω is the angular frequency. The other parameters have been defined before. The resulting parameters present an intuitive interpretation of the enhancement of charge transfer in CTS-based cells. Obviously, the fabricated CTS electrode satisfies one of the critical features for high-performance DSSCs in terms of its low charge transfer resistance ($R_{ct} \leq 3$ Ω cm^2).[53]

Stability is an important consideration when evaluating a CE. However, although a number of CEs with high-performance have been reported in recent years, there are actually very limited reports concerning their stability in the electrolyte.[54] To evaluate the electrochemical stability of our CTS electrode, an accelerated degradation EIS experiment was performed on their symmetrical cells. In Fig. 3d, the R_{ct} value derived from EIS spectra of the CTS was plotted as a function of the number of repeated EIS cycles. The inset presents the electrochemical behavior of CTS symmetrical cells with 19 complete EIS measurements. It was found that after the first EIS measurement, the R_{ct} value slightly increased from 0.45 to 0.55 Ω cm^2. Increased cycle number results in a continued increase in R_{ct}, but at a significantly slower rate, suggesting good electrochemical stability of the prepared CEs in the electrolyte. After 10 cycles of scan, the R_{ct} value of the CTS CE approached that of fresh Pt (0.75 Ω cm^2) and still maintained about 80% of its initial value after 19 cycles. The increase in the R_{ct} value, *i.e.*, the deactivation of the CE in I_3^-/I^- medium when subjected to repeated scanning of EIS was also observed in the case of standard Pt (Fig. S5†) except that the latter exhibits a slower decline rate. This deactivation was interpreted as being due to the poisoning effect of the catalyst.[55] To further advance the process of practical use, future work on enhancing the stability of CTS is required.

So far in this discussion, CTS has been shown to be more efficient than Pt in catalyzing the reduction of I_3^- to I^-, which can result in a considerable decrease in the charge transfer resistance of solar cells. However, it is worth noting that the experimental conditions for preparing such high-performance CEs have not yet been fully optimized, therefore further

enhancement in catalytic performance is still possible. According to previous studies, crystal structures, surface properties, as well as electrode morphologies play an important role in affecting the apparent catalytic performance of a film catalyst.[11,29,56] Therefore, two main processing parameters for thin film samples were targeted, *i.e.* the final annealing temperature and the concentration of the active layer on the FTO substrate. Fig. 4a presents the Nyquist plot of EIS with CTS dummy cells prepared at different annealing temperatures. For instance, T350 denotes a sample subjected to 350 °C annealing. The same goes for other samples. It was found that as the temperature rose in the range from 320 °C to 380 °C, the R_{ct} value slightly decreased from 0.45 Ω cm^2 to 0.39 Ω cm^2, indicating that the catalytic activity of the CTS CE was improved. However, when the annealing temperature was further increased from 380 °C to 440 °C, the catalytic activity of the CTS CE rapidly reduced as reflected by the abrupt increase of R_{ct} from 0.39 Ω cm^2 up to 1.1 Ω cm^2, indicating that the concentration of the active sites for catalytic reduction decreases with increasing annealing temperature. It is noted that the Raman spectra of these CTS did not show any noticeable change in peak position with varying annealing temperature (see Fig. S6†), phase-induced change in catalytic activity can thus be ruled out. The products were then subjected to XRD measurements. As shown in Fig. 4b, the width of the XRD diffraction peak gets narrow and the intensity increases with the increase of temperature (from 320 °C to 440 °C), which indicates the improved crystallinity of CTS thin films. The average crystallite sizes of the CTS particles determined using the Scherrer equation ($D = 0.941\lambda/\beta \cos\theta$, where D is the average grain size, λ is the X-ray wavelength (0.15405 nm), θ and β are the diffraction angle and full-width at half-maximum of an observed peak, respectively) are 20, 22, 25, 30, and 38 nm for T320, T350, T380, T410, and T440, respectively. This reminds us of a similar trend that was observed in the case of a graphene catalyst, where the decrease in catalytic activity was demonstrated when decreasing the number of defects in graphene, such as lattice defects, nitrogen-, oxygen-containing functional groups, *etc.* It was recognized that these defects act as the active sites and play a key role in catalyzing the reduction of I_3^- to I^-.[11,57,58] Therefore, in our case, similarly, we consider the possible decrease in defects with improving the crystallinity of the sample responsible for the decrease in catalytic activity. But any way, such a substantial dependence of catalytic activity on annealing temperature will deserve further investigation in the future.

On the basis of the optimized annealing temperature, we shall next study the effect of the mass loading of CTS on I_3^- reduction. The amount of the deposited CTS was controlled by varying the concentration of the used solution. Drop-casting the precursor solution with the same concentration can also lead to a greater loading. The CTS amount on each electrode is labeled arbitrarily as the corresponding optical absorbance of the active layer measured at the wavelength of 650 nm. For example, A16 denotes a sample for which the optical absorbance of the CTS layer

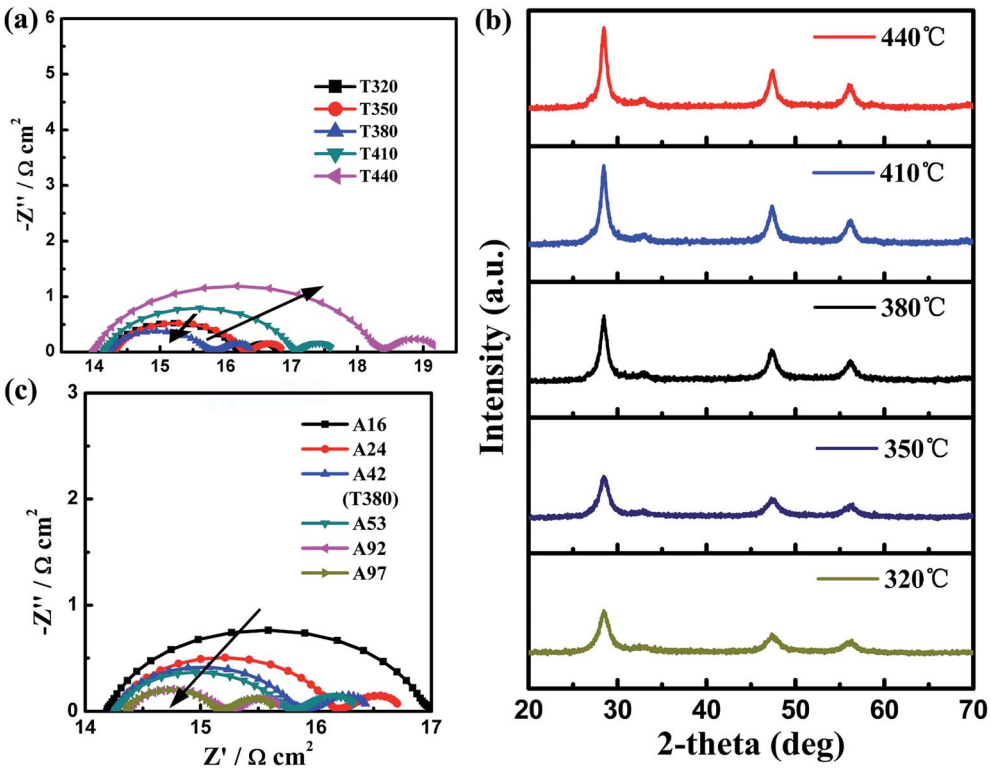

Fig. 4 (a) Nyquist plot of EIS measured on a dummy cell with CTS CEs prepared using different annealing temperatures (0.1 M precursor solution was used). (b) XRD patterns of the products annealed at different temperatures. (c) Nyquist plot of EIS measured on a dummy cell with CTS thin film of different optical absorbances.

measured at a wavelength of 650 nm is 16% (Fig. S7† gives their representative optical spectra; details about the procedure for preparing these electrodes are described in the caption of Fig. S7†). Fig. 4c shows Nyquist plots of EIS of dummy cells with various CTS electrodes. The R_{ct} value derived from EIS spectra is found to decrease with increasing optical absorbance, *i.e.*, the CTS mass loading on the FTO surface since absorbance is proportional to the concentration according to the Lambert–Beer law. The smallest R_{ct} value of about 0.22 Ω cm^2 was achieved on the A97 electrode which gives the highest optical absorbance among all. Such a great dependence of R_{ct} value on CTS loading can be explained by the fact that the electrocatalytic performance of a film catalyst is inherently related to its accessible surface area, *i.e.*, greater mass loading provides a higher number of catalytically active sites which facilitates the catalytic reaction on its surface. A similar trend was observed in previous studies but with different materials.[11,59] It is worth mentioning that the A97 electrode was prepared by a drop casting method using a 0.1 M precursor solution instead of the spin coating. In order to highlight the exclusive effect of CTS loading on its apparent catalytic performance, we have also prepared the A92 sample (by twice spin coating/sintering 0.2 M solution under the same heating conditions as A97) with the optical absorbance at 650 nm close to A97. Interestingly, A92 also demonstrated excellent catalytic performance that is nearly the same as that of A97, indicating that CTS loading on the FTO surface plays a dominant role in affecting its catalytic ability, independent of the approaches employed to load the CTS catalyst. The proportional increase in the catalytic performance of the CTS CE with the loading amount is similar to those found in Kavan *et al.*'s study, where a graphene CE with greater mass loading also demonstrated a higher electrocatalytic ability.[59] However, it is worth noting that if we compare our CTS to graphene CEs with similar catalytic abilities (*i.e.*, similar R_{ct} values), the mass loading in our case is nearly 12 times less than the one using graphene (*e.g.*, the A42 electrode gives $R_{ct} \approx 0.39$ Ω cm^2 with mass loading about 0.13 μg cm^{-2}, which is estimated from the concentration and the amount of the used precursor solution, while the graphene CE reaches about 1.5 μg cm^{-2}).[59]

Further, we tested the performance of our optimized CTS CE (A97) in iodine-mediated DSSCs with C101-sensitized TiO_2 photoanodes. The photocurrent–voltage (J–V) curves of the DSSCs obtained under 1 sun irradiation are shown in Fig. 5. The corresponding photovoltaic performance parameters are summarized in Table 1. The DSSC with the CTS CE yielded PCE with the maximum value of 10.26%, while the DSSC with the reference Pt CE produced a PCE of 9.31%. The increase of the efficiency is attributed to the improvement in fill factor, open-circuit photovoltage (V_{oc}), and short-circuit current density (J_{sc}). The series resistance (R_s) and shunt resistance (R_{sh}) of the solar cells were also simulated by the Oriel test station and are given in Table 1. The R_s, which is given by the equation $R_s = R_h + R_{ct} + Z_N$, affects the charge transportation within the solar cells and a small R_s will reduce the loss of the induced photovoltage; R_{sh} mainly reflects the efficiency of electron–hole separation compared with recombination in the photoanode and the increase in R_{sh} shall reduce the loss of photocurrent. Both of the

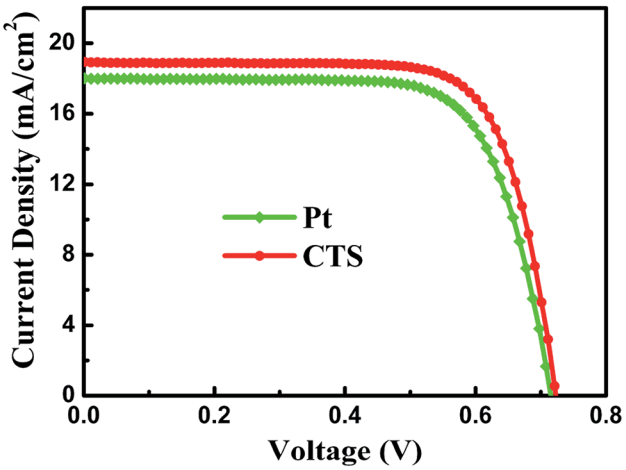

Fig. 5 Representative photocurrent-voltage curves of C101 dye-sensitized solar cells based on Pt and CTS electrodes (light intensity: 100 mW cm^{-2}, AM 1.5).

above circumstances will contribute to the increase in fill factor and thus the PCE.[60] However, we noticed that the R_{sh} values of these two cells are already in a nearly perfect level of approximately ten thousand ohms, meaning the recombination is efficiently controlled otherwise FF will be dragged downward. So the slight difference in R_{sh} would not be likely to cause such a notable change in J_{sc} (from 18.08 mA cm^{-2} of Pt to 19.26 mA cm^{-2} of CTS). Fig. S8† records the UV-vis optical reflection of CTS and Pt CEs using an integrating sphere. It shows that the reflection of light by the CTS CE is higher than that of Pt, suggesting its better light reflecting property to reduce the loss of the incident light. As a result, more light will be reflected back to the photoanode, more photo-generated electrons generated, which results in a higher J_{sc} value of the DSSC with the CTS CE. On the other hand, we attributed the slight increase in V_{oc} to the following two aspects. First, the increase in the shunt resistance (R_{sh}) will cause an increase in the V_{oc} according to the following equation:

$$\frac{V_{oc}}{R_{sh}} = I_L - I_0\left[\exp\left(\frac{qV_{oc}}{akT}\right) - 1\right] \quad (4)$$

where I_L, I_0, and a are the light generated current, diode saturation current, and ideality factor, respectively.[60,61] The other parameters have been defined before. Secondly, increase in the light generated current would generally cause increase in the V_{oc} according to the following equation:

$$V_{oc} = \frac{akT}{q}\ln\left(\frac{I_L}{I_0} + 1\right) \quad (5)$$

Therefore, the DSSC with the CTS CE showed an increased V_{oc} compared with that of the Pt CE.

The electrocatalytic activity of our CTS electrodes was finally compared with that of Pt in Co(III)/Co(II) electrolyte medium. EIS measurement was used to scrutinize the catalytic activity of these electrodes. In the previous I_3^-/I^- redox system, a great dependence of the catalytic performance on the annealing

Table 1 Photovoltaic parameters of the DSSCs with CTS and Pt CEs[a]

CE	V_{oc}/mV	J_{sc}/mA cm^{-2}	FF	η/%	R_s/Ω	R_{sh}/Ω
CTS	734 ± 3	19.26 ± 0.19	0.72 ± 0.01	10.18 ± 0.08	23 ± 2	11 078 ± 230
Pt	718 ± 2	18.08 ± 0.14	0.71 ± 0.01	9.24 ± 0.07	34 ± 3	9788 ± 180

[a] The above data are the average values obtained from 5 devices with standard deviation. Short circuit photocurrent density = J_{sc}, open-circuit voltage = V_{oc}, fill factor = FF, and solar conversion efficiency = η.

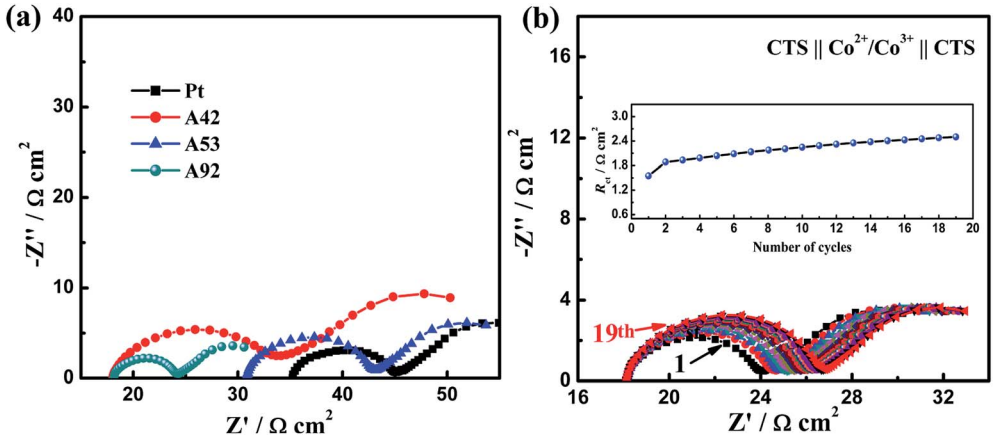

Fig. 6 (a) Nyquist plots from the EIS measurements of the Pt and CTS symmetrical cells (A42, A53, and A92) with a Co(III)/Co(II) redox electrolyte. The impedance spectra were acquired at an applied bias of 0 V, the modulation frequency ranging from 100 kHz to 0.01 Hz with a 5 mV ac amplitude. (b) Impedance plots of symmetrical cells with A92 subjected to accelerated degradation EIS scanning. The sequence of measurements was as follows: twice cyclic voltammetry scans from 0 V → 1 V → −1 V → 0 V (scan rate 50 mV s^{-1}) with a 20 s relaxation at 0 V followed by EIS measurement at 0 V from 100 kHz to 0.01 Hz. The inset shows the evolution of R_{ct} as a function of the number of cycles.

temperature and mass loading of the thin film catalyst was revealed. Interestingly, the same dependence holds also for the CTS CE in the Co(III)/Co(II) electrolyte system. Fig. 6a shows that reference symmetrical dummy cells with the Pt electrode achieve R_{ct} = 2.5 Ω cm^2, which compares favorably to those in another report.[59] It was found that the A92 electrode exhibited the smallest R_{ct} value of about 1.5 Ω cm^2, suggesting that the CTS electrode with optimized loading possesses a better catalytic ability and is more efficient in reducing the charge transfer resistance for the Co(III)/Co(II) electrolyte than Pt.

The electrochemical stability of the CTS CEs in the cobalt electrolyte was also tested. Fig. 6b shows the impedance plots of symmetrical cells with the CTS CE subjected to accelerated degradation EIS measurement. The inset shows the evolution of the R_{ct} value with respect to the number of EIS cycles. It is interesting to note that the changing trend of the R_{ct} value for CTS in Co(III)/(II) electrolyte medium resembles that of Pt in the same electrolyte media (Fig. S9†). Both electrodes show a quite low decline rate in catalytic performance. This suggests that CTS can also be a potential replacement for Pt in Co(III)/(II)-mediated DSSCs.

Conclusions

In summary, we have prepared highly uniform ligand-free CTS thin film electrodes composed of densely packed nanometer-sized grains, which exhibit remarkable electrochemical stability and electrocatalytic activity in both iodine and cobalt redox electrolytes. The catalytic activity of the CTS electrode was first theoretically predicted *via* first-principles calculations using DFT. On the basis of theoretical predictions, we have systematically investigated the feasibility of CTS thin film as a potential CE in DSSCs. Significantly, the CTS electrode with moderate mass loading enables an iodine electrolyte-mediated DSSC to yield photovoltaic performance of 10.26%, which is higher than that with the expensive Pt (9.31%). Further increasing the amount of CTS loading can markedly enhance its apparent catalytic performance toward both the reduction of I_3^- and Co^{3+}. The low cost of CTS, the excellent chemical stability, and its superior catalytic performance in both the important redox systems render it an ideal cathode candidate for DSSC applications. The results of this study thus represent an important step forward towards the development of low-cost Pt-free DSSCs.

Acknowledgements

This work was supported by the National Basic Research Program of China under Grant No. 2016YFA0202400, and the National Natural Science Foundation of China under Grant No. 51572080, 21403247, 21273242, 61404142, and 111 Project.

References

1 B. O'Regan and M. Grätzel, *Nature*, 1991, **353**, 737–740.

2 S. Mathew, A. Yella, P. Gao, R. Humphry-Baker, B. F. Curchod, N. Ashari-Astani, I. Tavernelli, U. Rothlisberger, M. K. Nazeeruddin and M. Grätzel, *Nat. Chem.*, 2014, **6**, 242–247.
3 A. Yella, H.-W. Lee, H. N. Tsao, C. Yi, A. K. Chandiran, M. K. Nazeeruddin, E. W.-G. Diau, C.-Y. Yeh, S. M. Zakeeruddin and M. Grätzel, *Science*, 2011, **334**, 629–634.
4 K. Kakiage, Y. Aoyama, T. Yano, K. Oya, J. Fujisawab and M. Hanaya, *Chem. Commun.*, 2015, **51**, 15894–15897.
5 J. H. Yum, E. Baranoff, F. Kessler, T. Moehl, S. Ahmad, T. Bessho, A. Marchioro, E. Ghadiri, J. E. Moser, C. Y. Yi, M. K. Nazeeruddin and M. Gratzel, *Nat. Commun.*, 2012, **3**, 631.
6 F. Bella, N. Vlachopoulos, K. Nonomura, S. M. Zakeeruddin, M. Gratzel, C. Gerbaldi and A. Hagfeldt, *Chem. Commun.*, 2015, **51**, 16308–16311.
7 F. Bella, S. Galliano, C. Gerbaldi and G. Viscardi, *Energies*, 2016, **9**, 384.
8 D. Zhou, Q. Yu, N. Cai, Y. Bai, Y. Wang and P. Wang, *Energy Environ. Sci.*, 2011, **4**, 2030–2034.
9 S. A. Sapp, C. M. Elliott, C. Contado, S. Caramori and C. A. Bignozzi, *J. Am. Chem. Soc.*, 2002, **124**, 11215–11222.
10 S. Shukla, N. H. Loc, P. P. Boix, T. M. Koh, R. R. Prabhakar, H. K. Mulmudi, J. Zhang, S. Chen, C. F. Ng, C. H. A. Huan, N. Mathews, T. Sritharan and Q. H. Xiong, *ACS Nano*, 2014, **8**, 10597–10605.
11 J. D. Roy-Mayhew, D. J. Bozym, C. Punckt and I. A. Aksay, *ACS Nano*, 2010, **4**, 6203–6211.
12 F. Hao, P. Dong, Q. Luo, J. B. Li, J. Lou and H. Lin, *Energy Environ. Sci.*, 2013, **6**, 2003–2019.
13 L. Li, J. Xiao, H. Sui, X. Yang, W. Zhang, X. Li, A. Hagfeldt and M. Wu, *J. Power Sources*, 2016, **326**, 6–13.
14 S. Ahmad, E. Guillen, L. Kavan, M. Gratzel and M. K. Nazeeruddin, *Energy Environ. Sci.*, 2013, **6**, 3439–3466.
15 V. Robles, J. F. Trigo, C. Guillen and J. Herrero, *J. Alloys Compd.*, 2015, **642**, 40–44.
16 S. A. Vanalakar, G. L. Agawane, A. S. Karnble, C. W. Hong, P. S. Patil and J. H. Kim, *Sol. Energy Mater. Sol. Cells*, 2015, **138**, 1–8.
17 M. Umehara, Y. Takeda, T. Motohiro, T. Sakai, H. Awano and R. Maekawa, *Appl. Phys. Express*, 2013, **6**, 045501.
18 J. Han, Y. Zhou, Y. Tian, Z. Huang, X. Wang, J. Zhong, Z. Xia, B. Yang, H. Song and J. Tang, *Front. Optoelectron.*, 2014, **7**, 37–45.
19 C. Z. Wu, Z. P. Hu, C. L. Wang, H. Sheng, J. L. Yang and Y. Xie, *Appl. Phys. Lett.*, 2007, **91**, 143104.
20 B. Qu, M. Zhang, D. Lei, Y. Zeng, Y. Chen, L. Chen, Q. Li, Y. Wang and T. Wang, *Nanoscale*, 2011, **3**, 3646–3651.
21 J. Xu, X. Yang, T.-L. Wong and C.-S. Lee, *Nanoscale*, 2012, **4**, 6537–6542.
22 X. K. Xin, M. He, W. Han, J. H. Jung and Z. Q. Lin, *Angew. Chem., Int. Ed.*, 2011, **50**, 11739–11742.
23 J. Y. Park, J. H. Noh, T. N. Mandal, S. H. Im, Y. Jun and S. I. Seok, *RSC Adv.*, 2013, **3**, 24918–24921.
24 W. Xu, X. Jiang, J.-M. Chen, R.-Q. Tan and W.-J. Song, *Acta Metall. Sin.*, 2015, **28**, 580–583.
25 Y. Yin and A. P. Alivisatos, *Nature*, 2005, **437**, 664–670.
26 M. V. Kovalenko, M. Scheele and D. V. Talapin, *Science*, 2009, **324**, 1417–1420.
27 J. Tang, K. W. Kemp, S. Hoogland, K. S. Jeong, H. Liu, L. Levina, M. Furukawa, X. H. Wang, R. Debnath, D. K. Cha, K. W. Chou, A. Fischer, A. Amassian, J. B. Asbury and E. H. Sargent, *Nat. Mater.*, 2011, **10**, 765–771.
28 Y. C. Wang, D. Y. Wang, Y. T. Jiang, H. A. Chen, C. C. Chen, K. C. Ho, H. L. Chou and C. W. Chen, *Angew. Chem., Int. Ed.*, 2013, **52**, 6694–6698.
29 H. Lee, S. E. Habas, S. Kweskin, D. Butcher, G. A. Somorjai and P. D. Yang, *Angew. Chem., Int. Ed.*, 2006, **45**, 7824–7828.
30 B. Bob, B. Lei, C. H. Chung, W. B. Yang, W. C. Hsu, H. S. Duan, W. W. J. Hou, S. H. Li and Y. Yang, *Adv. Energy Mater.*, 2012, **2**, 504–522.
31 T. K. Todorov, K. B. Reuter and D. B. Mitzi, *Adv. Mater.*, 2010, **22**, E156–E159.
32 D. H. Webber and R. L. Brutchey, *J. Am. Chem. Soc.*, 2013, **135**, 15722–15725.
33 X. K. Xin, M. He, W. Han, J. H. Jung and Z. Q. Lin, *Angew. Chem., Int. Ed.*, 2011, **50**, 11739–11742.
34 A. Weber, R. Mainz and H. W. Schock, *J. Appl. Phys.*, 2010, **107**, 013516.
35 F. Liu, J. Zhu, Y. Li, J. Wei, M. Lv, Y. Xu, L. Zhou, L. Hu and S. Dai, *J. Power Sources*, 2015, **292**, 7–14.
36 F. Liu, J. Zhu, L. Hu, B. Zhang, J. Yao, M. K. Nazeeruddin, M. Grätzel and S. Dai, *J. Mater. Chem. A*, 2015, **3**, 6315–6323.
37 E. B. Bi, H. Chen, X. D. Yang, W. Q. Peng, M. Gratzel and L. Y. Han, *Energy Environ. Sci.*, 2014, **7**, 2637–2641.
38 L. H. Hu, S. Y. Dai, J. Weng, S. F. Xiao, Y. F. Sui, Y. Huang, S. H. Chen, F. T. Kong, X. Pan, L. Y. Liang and K. J. Wang, *J. Phys. Chem. B*, 2007, **111**, 358–362.
39 G. Kresse and J. Furthmüller, *Comput. Mater. Sci.*, 1996, **6**, 15–50.
40 G. Kresse and J. Furthmüller, *Phys. Rev. B: Condens. Matter Mater. Phys.*, 1996, **54**, 11169–11186.
41 J. P. Perdew, K. Burke and M. Ernzerhof, *Phys. Rev. Lett.*, 1996, **77**, 3865–3868.
42 P. E. Blöchl, *Phys. Rev. B: Condens. Matter Mater. Phys.*, 1994, **50**, 17953–17979.
43 X.-a. Chen, H. Wada, A. Sato and M. Mieno, *J. Solid State Chem.*, 1998, **139**, 144–151.
44 Y.-T. Zhai, S. Chen, J.-H. Yang, H.-J. Xiang, X.-G. Gong, A. Walsh, J. Kang and S.-H. Wei, *Phys. Rev. B: Condens. Matter Mater. Phys.*, 2011, **84**, 075213.
45 P. Fernandes, P. Salomé and A. Da Cunha, *J. Phys. D: Appl. Phys.*, 2010, **43**, 215403.
46 D. Tiwari, T. K. Chaudhuri, T. Shripathi, U. Deshpande and V. Sathe, *J. Mater. Sci.: Mater. Electron.*, 2014, **25**, 3687–3694.
47 H. Guan, H. Shen, C. Gao and X. He, *J. Mater. Sci.: Mater. Electron.*, 2013, **24**, 1490–1494.
48 Y. Hou, D. Wang, X. H. Yang, W. Q. Fang, B. Zhang, H. F. Wang, G. Z. Lu, P. Hu, H. J. Zhao and H. G. Yang, *Nat. Commun.*, 2013, **4**, 1583.
49 W. Ke, G. Fang, H. Tao, P. Qin, J. Wang, H. Lei, Q. Liu and X. Zhao, *ACS Appl. Mater. Interfaces*, 2014, **6**, 5525–5530.

50 L. X. Yi, Y. Y. Liu, N. L. Yang, Z. Y. Tang, H. J. Zhao, G. H. Ma, Z. G. Su and D. Wang, *Energy Environ. Sci.*, 2013, **6**, 835–840.
51 X. J. Zheng, J. Deng, N. Wang, D. H. Deng, W. H. Zhang, X. H. Bao and C. Li, *Angew. Chem., Int. Ed.*, 2014, **53**, 7023–7027.
52 H. Wang, K. Sun, F. Tao, D. J. Stacchiola and Y. H. Hu, *Angew. Chem., Int. Ed.*, 2013, **52**, 9210–9214.
53 J. E. Trancik, S. C. Barton and J. Hone, *Nano Lett.*, 2008, **8**, 982–987.
54 S. N. Yun, P. D. Lund and A. Hinsch, *Energy Environ. Sci.*, 2015, **8**, 3495–3514.
55 A. Hauch and A. Georg, *Electrochim. Acta*, 2001, **46**, 3457–3466.
56 W. J. Xue, Y. F. Wang, P. Li, Z.-T. Liu, Z. P. Hao and C. Y. Ma, *Catal. Commun.*, 2011, **12**, 1265–1268.
57 H. Wang, K. Sun, F. Tao, D. J. Stacchiola and Y. H. Hu, *Angew. Chem.*, 2013, **125**, 9380–9384.
58 S. C. Hou, X. Cai, H. W. Wu, X. Yu, M. Peng, K. Yan and D. C. Zou, *Energy Environ. Sci.*, 2013, **6**, 3356–3362.
59 L. Kavan, J. H. Yum, M. K. Nazeeruddin and M. Gratzel, *ACS Nano*, 2011, **5**, 9171–9178.
60 Y. Jiang, B.-B. Yu, J. Liu, Z.-H. Li, J.-K. Sun, X. Zhong, J. Hu, W.-G. Song and L.-J. Wan, *Nano Lett.*, 2015, **15**, 3088–3095.
61 N. Koide, A. Islam, Y. Chiba and L. Han, *J. Photochem. Photobiol., A*, 2006, **182**, 296–305.